Papers

The impact of a non-uniform land surface on the radiation environment over an Arctic fjord – a study with a 3D radiative transfer model for stratus clouds over the Hornsund fjord, Spitsbergen*

Anna Rozwadowska[*]
Izabela Górecka[**]

Institute of Oceanology,
Polish Academy of Sciences,
Powstańców Warszawy 55, Sopot 81–712, Poland;

e-mail: ania@iopan.gda.pl;

[*]corresponding author,

[**]former affiliation

Abstract

This paper estimates the influence of land topography and cover on 3D radiative effects under overcast skies in the Arctic coastal environment, in particular in the

The complete text of the paper is available at http://www.iopan.gda.pl/oceanologia/

Hornsund fjord region, Spitsbergen. The authors focus on the impact of a non-uniform surface on: (1) the spatial distribution of solar fluxes reaching the fjord surface, (2) spectral shortwave cloud radiative forcing at the fjord surface, (3) the solar flux anomaly at the domain surface resulting from the assumption of a uniform surface, i.e. the error due to plane parallel assumptions in climate models, and (4) remote sensing of cloud optical thickness over the fjord. Their dependence on spectral channel, cloud optical thickness, cloud type, cloud base height, surface albedo and solar zenith angle is discussed. The analysis is based on Monte Carlo simulations of solar radiation transfer over a heterogeneous surface for selected channels of the MODIS radiometer. The simulations showed a considerable impact of the land surrounding the fjord on the solar radiation over the fjord. The biggest differences between atmospheric transmittances over the fjord surface and over the ocean were found for a cloud optical thickness $\tau = 12$, low solar zenith angle ϑ, high cloud base and snow-covered land. For $\tau = 12$, $\vartheta = 53°$, cloud base height 1.8 km and wavelength $\lambda = 469$ nm, the enhancement in irradiance transmittance over the fjord was 0.19 for the inner fjords and 0.10 for the whole fjord ($\lambda = 469$ nm). The land surrounding the Hornsund fjord also had a considerable impact on the spectral cloud radiative forcing on the fjord surface and the solar flux anomaly at the domain surface due to the uniform surface assumption. For the mouth and central part of the fjord the error due to the use of channel 2 of the MODIS radiometer ($\lambda = 858$ nm) for cloud optical thickness retrieval was < 1 in the case of low-level clouds (cloud base height 1 km, nadir radiance, $\vartheta = 53°$, cloud optical thickness retrieved solely from MODIS channel 2). However, near the shoreline (up to 2 km from it), especially over the inner fjords, the cloud optical thickness was then overestimated by > 3 for $\tau = 5$ and by > 5 for $\tau = 20$.

1. Introduction

Precise determination of solar radiation fluxes at the Earth's surface is crucial for a wide range of scientific problems, from primary production in the sea to climate change. Although the solar zenith angle is high in the Arctic, solar radiation is still an important source of heat there. Model studies of the sensitivity of the annual cycle of ice cover in Baffin Bay to short-wave radiation showed that during spring and summer the short-wave radiation flux dominated other surface heat fluxes and thus had the greatest effect on ice melt (Dunlap et al. 2007). Simulated ice cover is sensitive to the short-wave radiation formulation during the melting phase. According to Perovich et al. (2008) solar heating of the upper ocean was the primary source of heat for an extraordinarily large amount of melting at the bottom of the ice in the Beaufort Sea in the summer of 2007.

Solar radiation is also crucial for marine and sea ice algae. Light was considered to be the most probable factor controlling the onset of the spring ice-algal bloom in the lower part of the pack ice around Svalbard (Werner et al. 2007).

One of the components of the solar radiation flux at the Earth's surface is the radiation that reaches the surface after single or multiple reflections between the surface and the atmosphere. Its contribution to the total solar radiation flux at the surface depends closely on the reflective properties of the surface. In the Arctic, where the surface albedo may reach 0.9, the influence of the surface is important. For example, under stratus clouds of albedo $A_{cl} = 0.5$, the solar energy flux incident on a horizontally uniform flat surface covered with fresh snow (albedo $A_s = 0.9$) is about 80% higher than it would be on an ice-free sea surface. However, the energy absorbed by a snow-covered surface is less than the energy absorbed by a black one. In the above example, this would be 18% of the energy absorbed by the black surface. In terrestrial areas in the Arctic (Ny-Ålesund, Svalbard) the seasonal variability of the surface albedo along with the annual variation in the incoming light with polar night and polar day conditions and the atmospheric circulation are the factors which govern the natural variability of the short-wave and long-wave radiation fluxes (Ørbæk et al. 1999).

A plane parallel atmosphere over a flat and uniform surface is usually assumed in computations of solar radiation fluxes. This assumption can apply to the whole domain or to individual atmospheric columns (pixels). In the latter case negligible horizontal photon transfer between columns is additionally assumed. Such an approach is used in, for example, global circulation models (ICA – Independent Column Approximation) and remote sensing algorithms (IPA – Independent Pixel Approximation) (Marshak & Davis (eds.) 2005). Horizontal uniformity is also assumed when point measurements of solar radiation (ship-borne or from a coastal or inland station) are applied to the whole surrounding area. In polar regions, especially at the coasts, where the high surface albedo is accompanied by its high spatial variability, diverse topography and low solar altitudes above the horizon, the plane-parallel or ICA/IPA approaches result in considerable biases (McComiskey et al. 2006).

Both model analysis and measurements demonstrate the importance of horizontal photon transfer under a highly variable surface albedo. At a coastal high-latitude site, multiple reflections of photons between a high albedo surface and an overlying cloud can enhance the downwelling shortwave flux out over the adjacent open water to a distance of several kilometres (Lubin et al. 2002). Measurements from three radiometers deployed at different distances from the Palmer glacier (Antarctica) showed that under overcast layers which appear spatially uniform, a decreasing gradient occurs 86% of the time under the low overcast decks sampled.

The problems of the influence of high and variable surface albedo and/or diverse topography on solar radiation fluxes at the Earth's surface have been

studied for selected sites. 3D (three-dimensional) radiative transfer models, such as Monte Carlo (e.g. Kylling & Mayer 2001, Pirazzini & Räisänen 2008) and SHDOM (Spherical Harmonic Discrete Ordinate Method) (e.g. Degünther & Meerkötter 2000, Benner et al. 2001) are typically used in these analyses. Several authors have attempted the determination of bias in surface solar radiation fluxes under clear skies as a result of neglecting surface inhomogeneity, mainly topography, in Global Circulation Models (e.g. Chen et al. 2006, Liou et al. 2007). Rozwadowska & Cahalan (2002) analysed the biases in mean radiative fluxes at the surface and the TOA (Top Of the Atmosphere) for non-uniform sea ice and stratus cloud above it. Ricchiazzi & Gautier (1998) studied the impact of surface albedo inhomogeneity on cloud optical thickness retrievals from AVHRR measurements. Degünther & Meerkötter (2000) and Pirazzini & Räisänen (2008) studied the effect of albedo contrast on downward irradiance, including the effect of stratus cloud, for simplified model cases. Papers dealing with the impact of surface heterogeneity on radiative transfer in the high-latitude atmosphere are limited to the Antarctic environment, mainly the Palmer station (e.g. Podgorny & Lubin 1998, Ricchiazzi & Gautier 1998, Lubin et al. 2002, Ricchiazzi et al. 2002, McComiskey et al. 2006), continental Europe (Tromsø, Norway; Kylling et al. 2000, Kylling & Mayer 2001) or to sea ice (Smolskaia et al. 1999, Mayer & Degünther 2000, Benner et al. 2001, Rozwadowska & Cahalan 2002).

Because horizontal photon transport depends on both atmospheric and surface properties, the results obtained so far are of a regional nature and cannot be applied directly to regions of different topography, albedo distribution or prevailing atmospheric conditions. The Hornsund area (Spitsbergen, Svalbard) has a different, more mountainous relief, a more variable surface albedo distribution and a more complex coastline (a fjord) than the surroundings of the Palmer station. Very few works deal with the Spitsbergen area. Arnold et al. (2006) investigated the spatial and temporal variations in the surface energy balance of Midre Lovenbreen, a small valley glacier in northwest Spitsbergen, using a distributed, two-dimensional surface energy balance model. Glacier topography is found to play a fundamental role in determining the surface energy balance. Topographic shading, slope, as well as aspect and correction of the surface albedo for high solar zenith angles are found to play a crucial role in determining spatial patterns of surface energy balance and therefore melt. Szymanowski et al. (2008) developed a GIS-based clear sky solar radiation model for a part of the Hornsund area (SW Spitsbergen) covered by the orthophotomap 1:25 000 *Werenskioldbreen and surrounding areas* (Norsk Polarinstitutt and Silesian University). They applied the 'r.sun' solar model

(Hofierka 1997, Šúri & Hofierka 2004) to calculate daily sums of direct, diffuse and total 'clear-sky' solar radiation. Surface distributions of solar energy under clear sky conditions are highly variable in the area under study. Monthly mean total solar radiation fluxes under a clear sky in June vary from below 50 to over 350 W m^{-2}. The model by Szymanowski et al. (2008) is the only attempt to model the influence of the surface relief on solar radiation inflow to the Hornsund region. However, it covers only a small part of the area, is limited to clear sky conditions, and radiation transfer ('r.sun' model) is simplified compared to fully 3D radiative transfer techniques like Monte Carlo or SHDOM.

The aim of this paper is to estimate the influence of the land topography and cover on 3D radiative effects under overcast skies in the Arctic coastal environment, in particular in the region of the Hornsund fjord, Spitsbergen. The authors focus on the impact of a non-uniform surface on: (1) spatial distribution of solar fluxes reaching the fjord surface, (2) spectral cloud radiative forcing at the fjord surface, (3) the anomaly in surface irradiance resulting from the assumption of a uniform surface, and (4) remote sensing of cloud optical thickness over the fjord. The analysis is based on Monte Carlo simulations of solar radiation transfer over a heterogeneous surface for selected channels of a MODIS radiometer. The Hornsund region was selected for this study because of the research laboratory role it plays in the Arctic. For example, it is one of the flag sites for biodiversity studies. Glaciological and oceanographic studies have also been done there for many decades.

The outline of the paper is as follows. The models of the atmosphere, the surface topography and albedo as well as the Monte Carlo radiative transfer technique used in the simulations are presented in section 2, methods. Section 3 presents the results of the simulations, that is, surface distributions of the modelled irradiance transmittance and spectral cloud radiative forcing at the fjord surface, nadir radiances at the TOA over the fjord and the anomaly in the domain-averaged slope-parallel irradiance at the surface due to assumption of a uniform surface. Their dependence on spectral channel, cloud optical thickness, cloud type, cloud base height, surface albedo and solar zenith angle is discussed. Section 4 summarizes the conclusions.

2. Data and methods

2.1. Surface topography, land surface relief

Digitized 1:100 000 maps of Svalbard (UTM 33X projection, ellipsoid ED50, Norsk Polarinstitutt), sheets C13 Sorkapland, C12 Markhambreen and B12 Torellbreen as well as a Digital Elevation Model (Kolondra 2002)

and orthophotomap of Werenskioldbreen and surrounding areas, Spitsbergen, Svalbard (UTM 33X projection, ellipsoid WGS84, *Werenskioldbreen and surrounding areas* 2002) were used to develop a Digital Elevation Model (DEM) of the Hornsund area. A 200-metre cell grid was used as 'the ground' (the Earth's surface) in the radiative transfer model. The surface between four neighbouring grid nodes was approximated by the following function (Ricchiazzi & Gautier 1998):
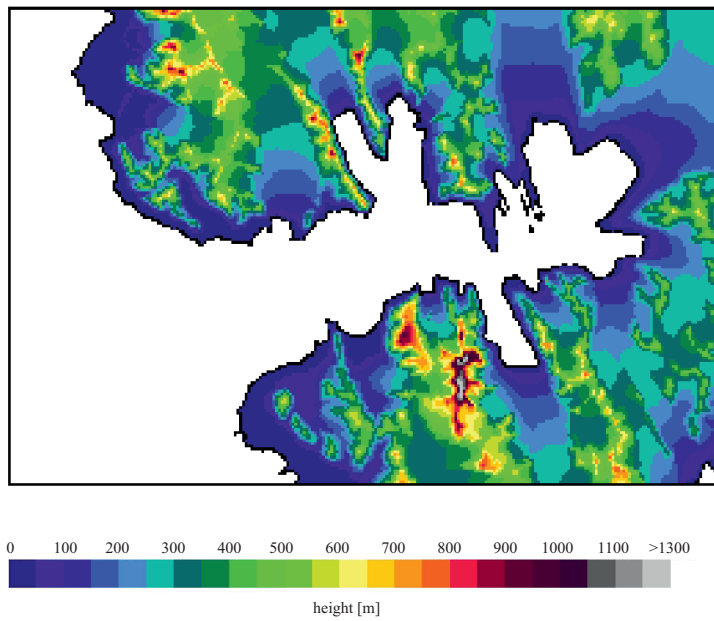
$$z = a_0\, x + a_1\, y + a_2\, x\, y + a_3\,, \qquad\qquad (1)$$

where x, y and z are the coordinates of a given point of a pixel (a grid cell) surface and a_0, a_1, a_2 and a_3 are coefficients fitted to the coordinates of the cell nodes. This approximation provides a continuous Earth's surface without unrealistic 'steps'. The working DEM of the Hornsund area covers an area of 51.40 km (X axis, W-E) $\times$ 34.40 km (Y axis S-N). The main domain (working area) was surrounded by a 20-kilometre-wide buffer belt to diminish possible computation bias due to the cyclic borders of the domain in the Monte Carlo simulations, which may happen in the case of large-scale non-uniformity of the domain. The width of the border was determined on the basis of numerical experiments for a cloud base height of 1.8 km, the highest cloud height value used in the study. The topography of the working area is presented in Figure 1.
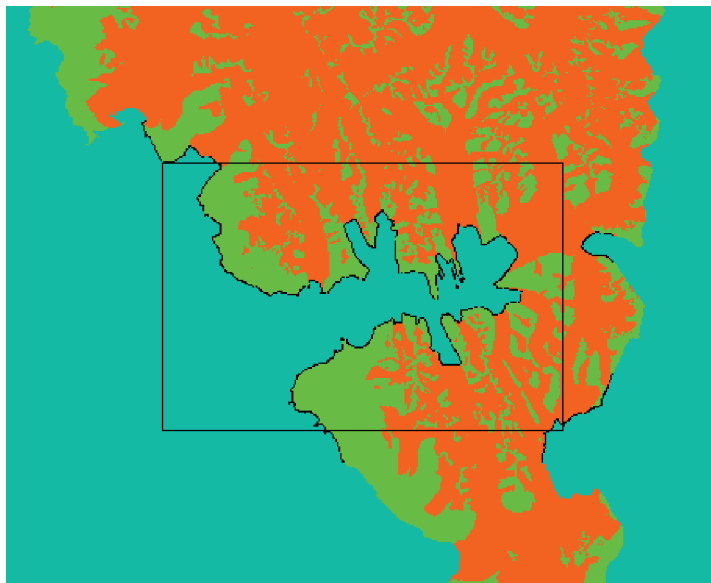
The latest updates of glacier front locations on the 1:100 000 maps of Svalbard come from 1990 for the northern coast of the Hornsund fjord and from 1961 for the southern coast; the updates for the Werenskioldbreen area are from 2002 (*Werenskioldbreen and surrounding areas* 2002). In this work the majority of glacier borders in the domain and the coastline were updated on the basis of a composed ASTER image (individual images from 2004 and 2005, projection UTM 33X, ellipsoid WGS 84, Błaszczyk et al. 2009).

2.2. Surface albedo parameterization

Based on digitized maps of Svalbard and the composed ASTER image, a dominant surface type was attributed to each grid cell: sea, glacier or tundra/rock (Figure 2). Two surface scenarios were used: 'summer' and 'spring'. In both cases the fjord and ocean are ice-free to maximize albedo contrast between the land and the sea. A flat water surface and specular reflection of photons from the water surface are assumed. Regardless of the land cover, the land surface is assumed to act as a Lambert reflector. The real bidirectional scattering functions are anisotropic, but previous simulations showed that the error introduced by this assumption is negligible
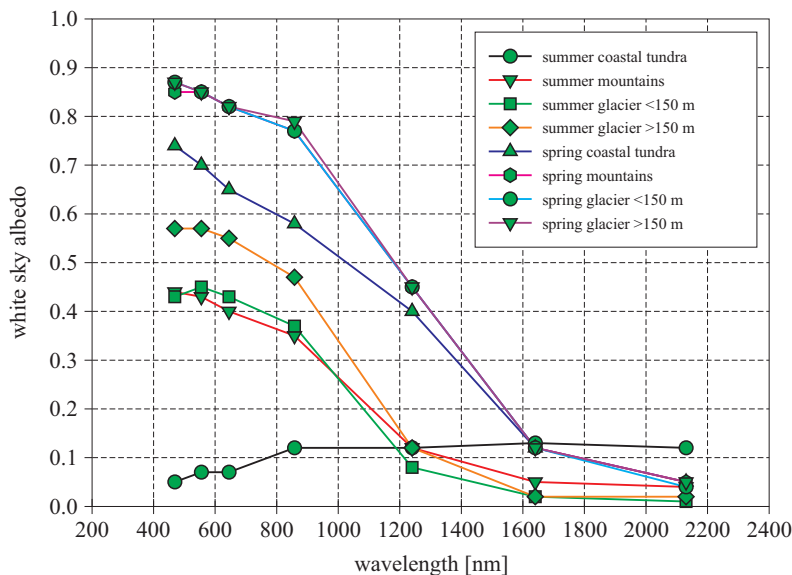
Figure 1. Topography (DEM) of the main domain

Figure 2. Types of surface used in the modelling. The main domain (working area) with the buffer belts is shown. Orange represents glaciers, green shows rocks and tundra, and cyan denotes the sea surface. The black rectangle is the border of the main domain

in flux simulations (Rozwadowska & Cahalan 2002). Albedo values for MODIS channels 1–7 for tundra, glacier ice and snow were taken from MODIS albedo products for a white sky: the 105th day of 2007 for the spring case with 'winter-like' snow and the 225th day of 2006 for the summer with a minimum albedo.

The surface distributions of the actual white sky albedo (images) could not be used directly because the images were partly cloudy. Therefore, modal values of albedo frequency distributions were adopted as representative of a given surface type. The lower and higher parts of glaciers as well as coastal tundra and mountains were treated separately. The height of separation (division) between the lower and higher parts of glaciers as well as between the coastal tundra and mountains was determined from dependences of the albedo on terrain elevation, obtained from MODIS images. The height of separation was set at 150 m. The spectral albedo of selected types of surface used in the modelling is given in Figure 3. In early spring, all the land is covered with snow. The coastal tundra, however, shows a lower albedo than the glaciers and mountains. Snow on the coast is transformed, and in some places it may be blown away, leaving the ground covered with ice. The albedo of snow-covered glaciers and mountains is slightly lower than that of fresh snow (cf. Grenfell & Perovich 1984, Grenfell et al. 1994, Arnold et al. 2002). This can be attributed to the

Figure 3. Spectral albedo (MODIS SW channels) of the surface types used in the modelling

transformation of the snow surface and the uneven surface (e.g. sastrugi). In summer, the coastal (low) tundra consists of vegetation, various fractions of material accumulated by glaciers, ponds and damp areas. Its albedo is lower than that of typical tundra vegetation and closer to the albedo of moraines measured in Spitsbergen (Winther et al. 1999, Arnold et al. 2002). It is consistent with albedo measurements performed at the Hornsund station in summer 2007. The mountain surface in summer is a mixture of patches of old snow and bare rock. The glacier albedo is much lower than in spring. The lower parts of glaciers are largely deprived of snow. The snow cover in the higher parts of glaciers is strongly transformed, may be wet and covered with puddles of water.

2.3. Atmosphere

The model atmosphere is 60 km high and is divided into 7 homogeneous layers: 0–1,1–2, 2–3, 3–5, 5–10, 10–20, 20–30 and 30–60 km. The optical thickness of the topmost layer (30–60 km) is equal to the optical thickness of the 30–100 km layer in the Modtran 4 Subarctic Summer atmospheric model (Berk et al. 2003). The presence of a cloud layer increases the number of layers to 8 or 9, depending on cloud thickness and position.

Gas absorption was neglected in the simulations to speed up the computations. The calculations were performed for MODIS bands 1–7, which are outside major absorption bands. Therefore, radiation is attenuated mainly by clouds. Neglecting gas absorption resulted in overestimation of the downward irradiance at the sea surface from 2% (solar zenith angle $\vartheta = 53°$) to 4% ($\vartheta = 79°$) for $\lambda = 469$ nm (ozone absorption) and from 7% ($\vartheta = 53°$) to 13% ($\vartheta = 79°$) for $\lambda = 858$ nm (water vapour absorption). The magnitude of uncertainty in nadir radiance as a result of neglecting gas was typically $< 2\%$ for these cases. Comparisons were performed for a cloudless atmosphere over water. The Rayleigh scattering and aerosol attenuation profiles used in the comparisons were the same as in the simulations of a cloudy atmosphere presented later in this paper.

The Rayleigh scattering coefficient was parameterized using the Callan formula (after Thomas & Stamnes 2002) and profiles of air temperature and pressure from Ny-Ålesund, Spitsbergen, obtained in May 2007. The radio sounding data from Ny-Ålesund were provided by AWI. For altitudes higher than 30 km, averaged profiles for Subarctic Summer and Winter (Berk et al. 2003) were used.

Up to 3 km, the 'Arctic July' model aerosol and Arctic aerosol profile shape from d'Almeida et al. (1991) were used. For the higher layers, tropospheric (3 to 10 km) and stratospheric (10 to 30 km) aerosol models from Modtran were adopted (Berk et al. 2003). The aerosol optical

properties used in Monte Carlo simulations are the attenuation coefficient, single scattering albedo and asymmetry factor of the scattering phase function. The mean humidity profile from Ny-Ålesund (April to September 2007) was used to determine aerosol properties.

The aerosol scattering phase function was estimated using the Henyey-Greenstein function (Henyey & Greenstein 1941). Model calculations were performed for horizontal visibility $= 60$ km and aerosol optical thickness AOT(555 nm) $= 0.08$.

In all simulations clouds were represented by a uniform layer of water cloud. Since we did not find any statistics of optical properties of water clouds from Spitsbergen, the properties of clouds were selected on the basis of measurements from Barrow, Alaska (Dong & Mace 2003) and the SHEBA station (Shupe et al. 2001, 2005). We assumed that Spitsbergen clouds were closer to the clouds over Barrow than over the SHEBA ice camp (high Arctic). In our simulations, the liquid water content of clouds LWC $= 0.19$ g m^{-3} and the droplet effective radius $r_e = 10$ μm. Cloud optical properties, i.e. attenuation coefficient, single scattering albedo and asymmetry factor of the phase function, were computed using a climatological parameterization of the spectral optical properties of water clouds by Hu & Stamnes (1993). The parameterization relates optical properties to r_e and the liquid water path.

In most of the runs/simulations, clouds had an optical thickness τ(555 nm) $= 12$ and thickness 0.4061 km. For comparison, at Barrow, from May to September, the monthly mean effective radius of single-layer overcast low-level stratus clouds ranges from 8 to 13 μm, monthly mean LWC varies from 0.24 to 0.31 g m^{-3}, the mean τ(555 nm) varies from 9 to 18, the mean cloud base height varies from 0.3 to 1.1 km, and the mean cloud thickness is 0.4 km (Dong & Mace 2003). At the ice camp of the SHEBA experiment, monthly mean r_e was within the range 6 to 7 μm (March to September), and LWC varied from 0.07 to 0.11 g m^{-3} (Shupe et al. 2005).

2.4. Radiative transfer model

Radiative transfer in the 3D Arctic atmosphere was modelled by a 3D Monte Carlo code, using the 'maximum cross-section method' of Marchuk et al. (1980). The original code developed by Marshak et al. (1995) was modified in this work. The reflection and absorption of photons by the Earth's surface of variable topography and albedo was added. The Monte Carlo 'maximum cross-section method' code was tested against DISORT (Stamnes et al. 1988, 2000) for a wide range of uniform cases. Absolute differences between transmittances calculated by both methods did not exceed 0.001.

The forward Monte Carlo method was used for flux and radiance computations: slope-parallel irradiance and (net) irradiance at the surface and nadir radiance at the TOA. A photon was traced until it reached the TOA, or was absorbed by the Earth's surface or by the atmosphere.

When a photon went below the highest elevation of the terrain, it was checked for intersection with the surface. The photon was reflected or absorbed in the first pixel (k,l) along the photon path, for which the point of intersection of the photon path with the surface (equation (1) with coefficients a_0, a_1, a_2 and a_3 for the pixel (k,j)) was within limits of this pixel (Ricchiazzi & Gautier 1998, Rozwadowska 2008). The new direction of the photon after reflection was determined with respect to the normal to the surface at the point of intersection. A detailed description of the mathematical solution of this problem is given in Mayer et al. (2010).

A technique called 'Russian roulette' was applied to a photon of weight < 0.5 to speed up computations (Iwabuchi 2006). The photon disappeared when its weight was less than a random number, otherwise its weight was set to 1.

The radiance measured by a satellite instrument was simulated using the 'local estimation' technique (Marchuk et al. 1980, Iwabuchi 2006). The radiance measured by a satellite is represented by the normalized radiance and given by the sum of all scattering events i of photon j in the atmospheric column (k,l) within the domain, divided by the number of photons incident at the top of this column N_{TOA}, and multiplied by π (adopted from Spada et al. 2006):

$$I = \frac{\pi}{N_{\mathrm{TOA}}} \sum_{j=1}^{N_{\mathrm{TOA}}} \sum_{i=1}^{N_{\mathrm{sca}}(j)} I_{i,j} \,. \tag{2}$$

The relative slope-parallel irradiance at the Earth's surface E_s^{rel} was computed according to the following equation:

$$E_s^{\mathrm{rel}} = \frac{E_s}{E_{\mathrm{TOA}}} = \frac{A_p}{A_s \, N_{\mathrm{TOA}}} \sum_{j=1}^{N} w_j \,, \tag{3}$$

where E_s is the slope-parallel irradiance at the Earth's surface in a pixel/column (k,l), E_{TOA} is the solar irradiance at the TOA, N_{TOA} is the number of photons incident at the top of the atmospheric column (k,l), A_s is the area of the Earth's surface within the pixel/column (k,l), A_p is the area of the

pixel (k, l), N is the number of photons reaching the Earth's surface within the pixel/column (k, l), and w_j is the weight of the j-th photon reaching the Earth's surface within the pixel/column (k, l). For a horizontal surface, like a fjord, the open ocean or flat land surfaces, the slope-parallel irradiance E_s is the downward irradiance E_d and the relative slope-parallel irradiance is the atmospheric transmittance of the downward irradiance T_E.

The relative slope-parallel net-irradiance $E_{\text{net}}^{\text{rel}}$ was computed analogously to the relative slope-parallel irradiance except that only photons absorbed by the surface were counted, so N in equation (3) would mean the number of photons absorbed by the Earth's surface within the pixel/column (k, l), and w_j would be the weight of the j-th photon absorbed by the Earth's surface within the pixel/column (k, l).

Random numbers were generated with a KISS number generator (Marsaglia & Zaman 1993, Marsaglia 1999; http://www.fortran.com/kiss. f90).

Table 1. List of non-uniform Monte Carlo simulations performed in this work. The wavelengths are the central wavelengths of the MODIS channels for which simulations were performed. $g = 0.75$ indicates a run with a modified value of the asymmetry parameter of the scattering phase function

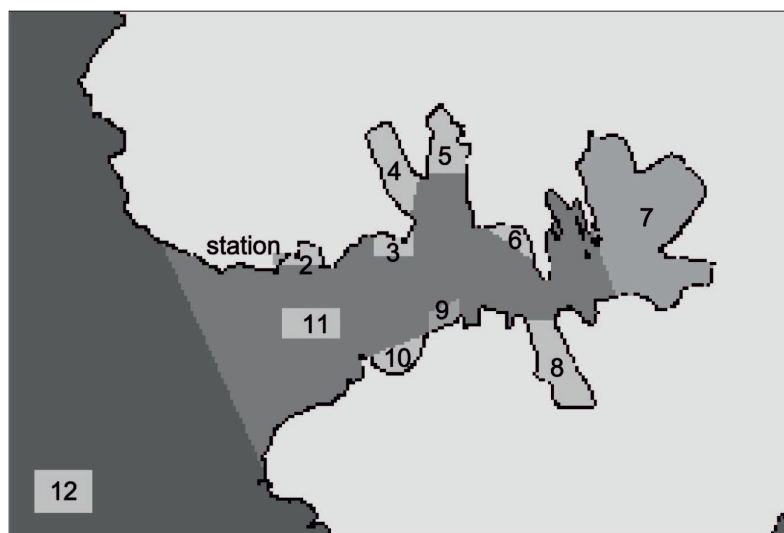| Cloud optical thickness	Cloud thickness [km]	Cloud base height [km]	Solar zenith angle [deg]	Solar azimuth [deg]	Surface albedo type	Wavelength [nm]
0			53	180	spring	469, 858, 1240
0			53	180	summer	469
0			66, 79	180	spring	469
0			79	0	spring	469, 858, 1240
0			66	90	spring	469, 858, 1240
0			66	270	spring	469, 858, 1240
5	0.169	1	53	180	spring	469, 858
12	0.406	1	53	180	spring	469, 858, 1240, 1640
12	0.406	1	53	180	summer	469
12	0.406	1	53	180	spring	469, $g = 0.75$
12	0.406	0.2	53	180	spring	469
12	0.406	1.8	53	180	spring	469
12	0.406	1	66	180	spring	469, 858
12	0.406	1	79	180	spring	469, 858
12	0.406	1	79	0	spring	469, 858, 1240
12	0.406	1	66	90	spring	469, 858, 1240
12	0.406	1	66	270	spring	469, 858, 1240
20	0.677	1	53	180	spring	469, 858
30	1.015	1	53	180	spring	469, 858

2.5. Simulations

We did the computations for selected MODIS channels: 3 (459–479 nm), 2 (841–876 nm), 5 (1230–1250 nm) and 6 (1628–1652 nm).

In most cases the cloud layer was assumed to be 1000 m above sea level, which is higher than most mountains. The elevation of the highest peak in the area, Hornsundtind, is 1431 m. The cloud optical thickness in the simulations was typically set to 12. The full list of numerical simulations is given in Table 1. The number of photons used in a single run varied from 10^6 for plane parallel cases to 2×10^9 for most non-uniform cases.

3. Results and discussion

This section presents the surface distributions of the modelled relative irradiance (transmittance) and spectral cloud radiative forcing at the fjord surface and nadir radiances at the TOA over the fjord and the anomaly in domain-averaged irradiance due to the assumption of surface uniformity. Their dependence on spectral channel, cloud optical thickness, cloud base height and solar zenith angle is discussed.

In order to analyse the influence of various factors on the surface distribution of the surface irradiance and TOA radiance, 14 test plots were selected in the fjord and the adjacent ocean (Figure 4). Plot 1 is the Hornsund station area. It is a land plot, shown here for comparison with
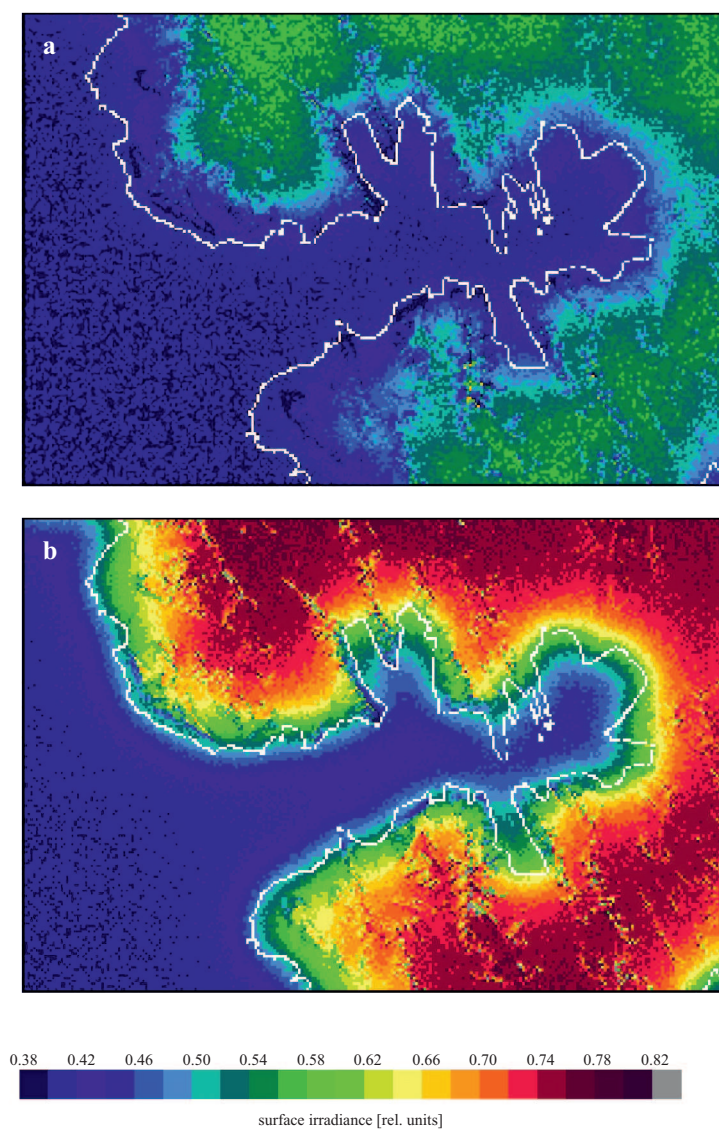

Figure 4. Selected areas (plots) for which the modelling data are averaged

the modelling results for the fjord. Solar radiation measurements have been carried out at the station for many years. Plots 8–11 lie along the southern shore of the fjord. Plot 10 (Gashamna) is an embayment with over 700-metre high mountains to the east and the receding front of the Gasbreen glacier to the south. Plot 9 abuts the over 600 metre-high cliff of Rasstupet. Plot 8 is a fjord with a north-south axis (Samarinvagen) bordered by mountains and terminated by glaciers. These areas have their equivalents along the northern shore: an embayment (Isbjornhamna with Hansbukta – 2), fields adjacent to the mountain cliff (Gnalberget – Sofiebogen – 3, Adriabukta – Hyrnefjellet – 6) and glacier-ended fjords (eastern Burgerbukta – 4 and western Burgerbukta – 5). Western Burgerbukta is surrounded by mountains with 700–900 metre-high peaks. Plot 7 is the easternmost part of the Hornsund bordered by glaciers. Plot 11 represents the central part of the western Hornsund. Plot 12 is the ocean area, where terrestrial influences are few if any. The increase in irradiance (transmittance) in this plot can, at least partly, result from the cyclic borders of the 'broad' domain. The broad domain is the working domain with the buffer belts. The bias in the results due to the cyclic borders of the domain does not exceed the difference in irradiance (transmittance) between a horizontally uniform atmosphere over a horizontally uniform ocean (open ocean conditions) and plot 12.

3.1. Surface irradiance

Figure 5 shows examples of the relative downward irradiance or irradiance transmittance T_E distribution at the fjord surface for a cloud layer of $\tau = 12$ with its base at 1 km above sea level for the spring and summer albedo patterns for $\lambda = 469$ nm (MODIS channel 3). The solar position, the zenith angle $\vartheta = 53°$ and the azimuth $\alpha = 180°$, are for noon on 21 June. The solar zenith angle $\vartheta = 53°$ is the smallest such angle in the Hornsund area. The irradiance transmittance on the open ocean surface under the same conditions is 0.40. Under spring albedo conditions an increase in transmittance is observed over the whole fjord. The greatest enhancement $\Delta T_E = 0.15$–0.16 (enhancement relative to the transmittance over the ocean $\Delta T_E^{\mathrm{rel}} = 37$–40%) is found for the inner fjords surrounded by steep mountains (plots 4, 5 and 8). The lowest $\Delta T_E^{\mathrm{rel}} = 6\%$ is at the mouth of the fjord (plot 11). The mean T_E for the whole fjord is 0.475, that is 119% of the 'ocean' value and is similar to the values for areas close to the nearly straight coastline with cliffs (without bays) (plots 3 and 9). The atmospheric transmittance at the station and at the Isbjornhamna surface (plot 2) is relatively high, $T_E = 0.53$, 12% higher than the mean transmittance for the fjord. These proportions are representative of the visible part of the spectrum. For the summer albedo pattern and a cloud layer of $\tau = 12$
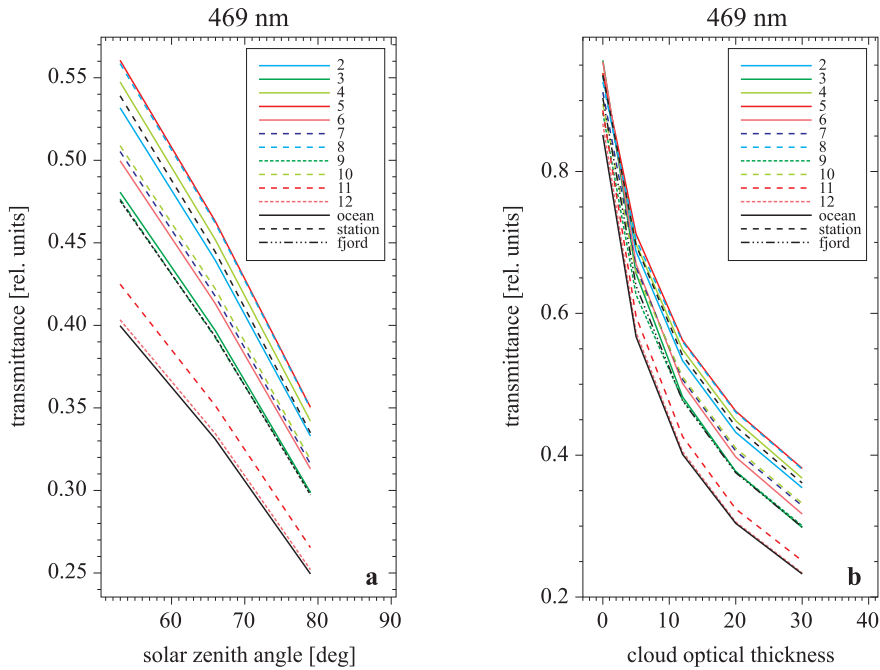
Figure 5. Examples of relative slope-parallel irradiance distribution at the fjord surface for a cloud layer of $\tau = 12$ with its base at 1 km above sea level for the summer (a) and spring (b) albedo patterns, $\lambda = 469$ nm (MODIS channel 3), $\vartheta = 53°$ and $\alpha = 180°$. For horizontal surfaces (e.g. water) the relative slope-parallel irradiance is the atmospheric transmittance

situated 1 km above the fjord, the transmittance enhancement over the fjord is much less. T_E ranges from 0.44–0.45 ($\Delta T_E^{\mathrm{rel}} = 11\%$) for the inner fjords closed off by a glacier to 0.41–0.42 ($\Delta T_E^{\mathrm{rel}} = 4\%$) for rock cliffs. The

value $\Delta T_E^{\text{rel}} = 4\%$ ($T_E = 0.42$) is also representative of the whole fjord. At the mouth of the fjord, the transmittance enhancement is negligible for the summer albedo pattern.

For opaque clouds ($\tau = 12$, $h = 1$ km, spring albedo pattern, $\lambda = 469$ nm and $\alpha = 180°$) the relative enhancement in transmittance is practically independent of solar position and is nearly constant for ϑ from 53° to 79° (Figure 6a). T_E, however, decreases with increasing ϑ, from 0.56 (the inner fjords) – 0.40 (the ocean) for $\vartheta = 53°$ to 0.35–0.25 for $\vartheta = 79°$.

Figure 6. Dependence of irradiance transmittance distribution at the fjord surface on solar zenith angle and cloud optical thickness; simulations for a cloud layer with its base at 1 km above sea level, spring albedo pattern, $\lambda = 469$ nm (MODIS channel 3), $\alpha = 180°$ and $\tau = 12$ (a) and $\vartheta = 53°$ (b). The numbers in the legend are the plot numbers from Figure 4

An increase in cloud optical thickness results in increasing ΔT_E^{rel} (simulations for $\vartheta = 53°$, $h = 1$ km, spring albedo pattern and $\lambda = 469$ nm), which is illustrated in Figure 6b. This is because the cloud albedo rises with τ. For $\tau = 30$, $\Delta T_E^{\text{rel}} = 65\%$ for the inner fjords (plots 5 and 8) and $\Delta T_E^{\text{rel}} = 29\%$ for the whole fjord. The maximum transmittance enhancement $\Delta T_E = 0.16$ is found for the inner fjords and $\tau = 12$. For the whole fjord the maximum $\Delta T_E = 0.075$ is also found for $\tau = 12$. For a cloud optical thickness ranging from 5 to 30, ΔT_E for each individual plot changes by
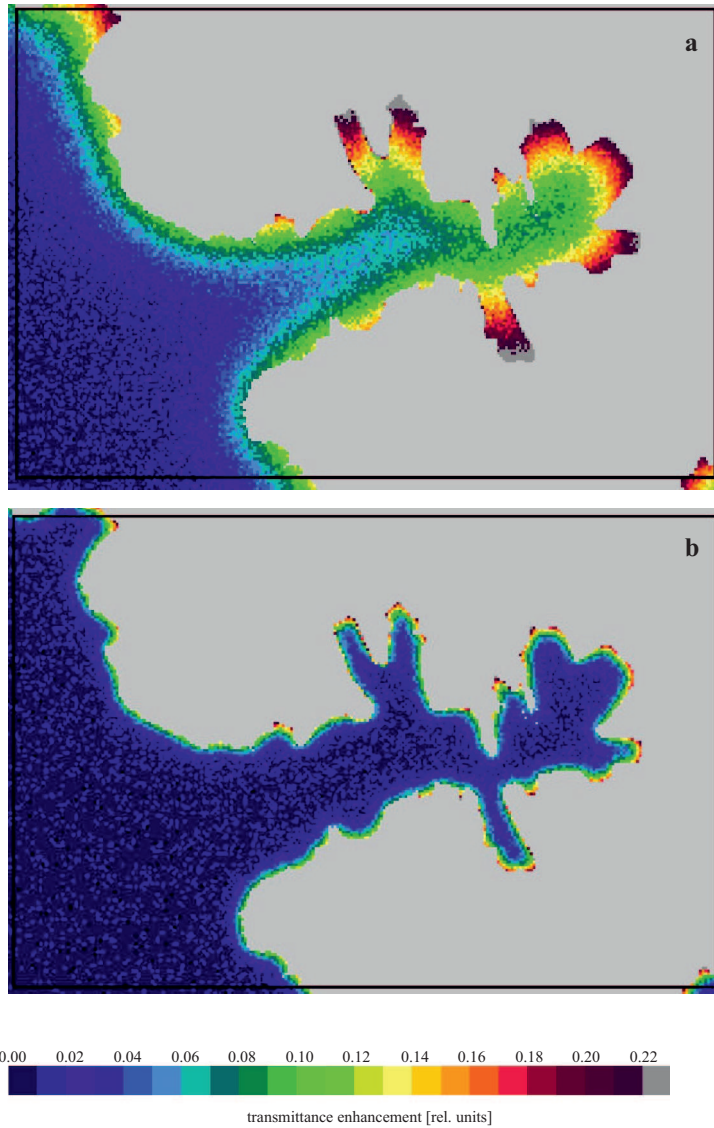
< 0.02, which is much less than the spatial variability of ΔT_E. The spatial distribution of T_E is azimuthally independent for $\tau \geq 12$ (not shown in the figures). The sky radiance is then sufficiently independent of the azimuth. The irradiance on parts of the land that are above the cloud layer or in the cloud is an exception. Under a cloudless sky and optically thin clouds ($\tau = 5$) the angular distribution of the incoming solar radiation depends on the sun's position in the sky. Shading by the mountains and reflection of 'direct' light from the snow-covered cliffs facing the sun (plots 3 and 6) occurs. In the central part of the fjord and for snowy cliffs, ΔT_E is the highest for a cloudless sky.

Cloud base height is an important factor influencing atmospheric transmittance over the fjord. Given constant cloud and surface reflectivities, cloud height determines the horizontal distance a photon can travel in the atmospheric layer between the surface and the cloud layer base. In a mountainous region like the Hornsund area, mountains additionally limit the horizontal path of photons, especially when the cloud base is below the mountain peaks. This attenuates the irradiance transmittance, both the increase over the fjord waters and the decrease over the land, which is shown in Figure 7 for the cases of $h = 200$ m and $h = 1800$ m ($\tau = 12$, spring albedo pattern, $\vartheta = 53°$ and $\lambda = 469$ nm). For $h = 200$ m, the irradiance transmittance over the fjord nearly reaches its 'oceanic' value within 2 km from a straight shore, while for $h = 1800$ m the ocean value is never reached over the ca 10-km-wide fjord. The transmittance enhancement over the near-shore plots (Figure 8a) is 1.5–3 times lower for $h = 200$ m than it is for $h = 1800$ m. ΔT_E drops 7 times with diminishing cloud layer height in plot 11 (the fjord mouth), and 3 times over the whole fjord. The radiative conditions are more local for lower clouds, and dark water diminishes irradiance transmittance at the coast. Hence, irradiance transmittance at the station drops with increasing cloud base height.
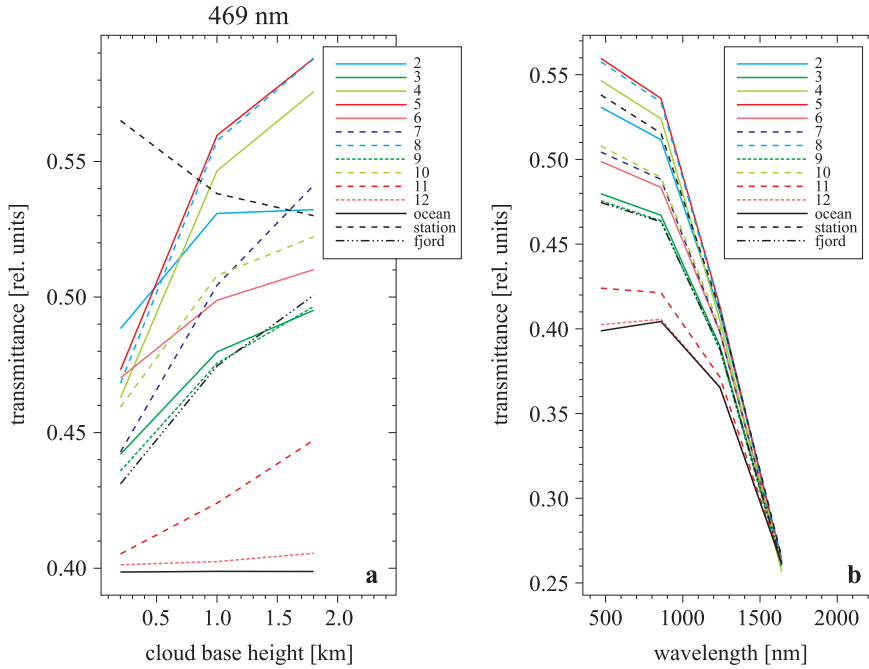
The transmittance enhancement over the fjord due to 3D effects (photon transport) weakens in the infrared. It is practically negligible for $\lambda = 1640$ nm (Figure 8b), the absolute value of ΔT_E is lower than 0.005 for all the plots. In this spectral channel the surface albedo is almost uniform and very low (< 0.11).

Because the 3D effects depend strongly on wavelength, they must modify the irradiance spectrum on the fjord surface. The behaviour of the ratio $T_E(\lambda = 469 \text{ nm})/T_E(\lambda = 858 \text{ nm})$ with increasing τ is presented in Figure 9. The differences in the ratio between the fjord and the ocean are the highest for inner fjords (plots 5 and 8) and they range from 0.08 for a cloudless sky to 0.66 for clouds of $\tau = 30$ ($h = 1$ km, spring albedo pattern, $\vartheta = 53°$ and $\lambda = 469$ nm). The respective ratio differences for the whole fjord are

Figure 7. Distributions of irradiance transmittance enhancement $T_E - T_E(\text{ocean})$ at the fjord surface for different cloud base heights: 1800 m (a) and 200 m (b). The other input parameters were the same in both simulations: a cloud layer of $\tau = 12$, spring albedo pattern, $\lambda = 469$ nm (MODIS channel 3), $\vartheta = 53°$ and $\alpha = 180°$. The land is masked
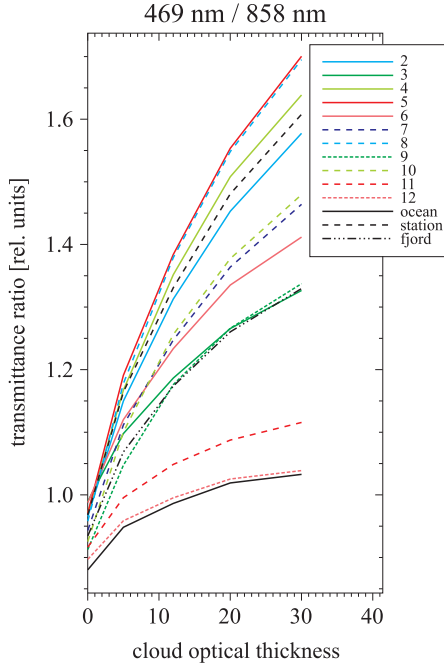
0.05 and 0.29. The variability of $T_E(\lambda = 469 \text{ nm})/T_E(\lambda = 858 \text{ nm})$ over the fjord are caused mainly by a decrease in snow albedo with the wavelength between $\lambda = 468$ nm and 858 nm.

Figure 8. Dependence of irradiance transmittance distribution at the fjord surface on cloud base height and solar radiation wavelength (MODIS channels); simulations for $\tau = 12$, $\vartheta = 53°$, $\alpha = 180°$, spring albedo pattern, and $\lambda = 469$ nm (a), and cloud base height $h = 1000$ m (b). The numbers in the legend are the plot numbers from Figure 4

All the runs/simulations discussed so far represent radiative transfer through water clouds. So as to simulate 3D effects under ice clouds, the asymmetry factor g was changed from 0.865 used for water cloud simulations with $\lambda = 469$ nm to 0.75 (e.g. Zhang et al. 2002, Baran et al. 2005, Fu 2007). An 'ice cloud' run was performed for the spring albedo pattern, $\tau = 12$, $\vartheta = 53°$, $h = 1$ km and $\lambda = 469$ nm (not shown in the figure). It was found that for ice clouds the 3D effect is stronger than for water clouds of the same height and optical thickness. Lowering factor g increases cloud albedo and decreases its transmittance. Thus it reduces T_E but increases ΔT_E^{rel} from 19% for $g = 0.865$ to 25% for $g = 0.75$ for the whole fjord, and from 40% to 55% for the inner fjords (plots 5 and 8).

Summing up, the figures show that the spatial variability in relative transmittance enhancement ΔT_E^{rel} is the highest for a high land surface albedo (high albedo contrast between the land and the water), thick clouds ($\tau = 30$) with a high base; ΔT_E, however, is the highest for $\tau = 12$ and a low solar zenith angle in our simulations.

469 nm / 858 nm

Figure 9. Dependence of the ratio $T_E(\lambda = 469 \text{ nm})/T_E(\lambda = 858 \text{ nm})$ at the fjord surface on cloud optical thickness; simulations for cloud base height $h = 1000$ m, $\vartheta = 53°$, $\alpha = 180°$, spring albedo pattern and $\lambda = 469$ nm. The numbers in the legend are the plot numbers from Figure 4
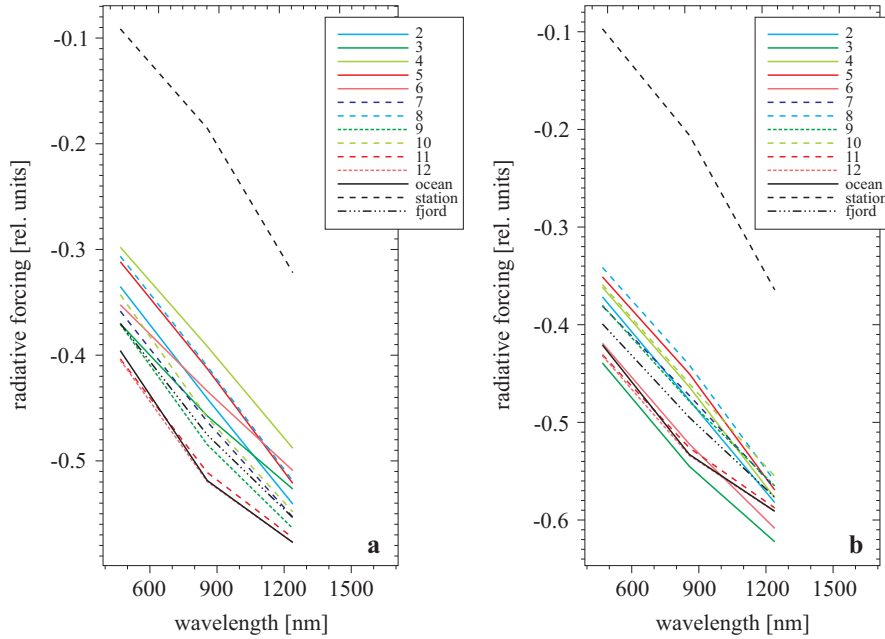
3.2. Cloud radiative effect

Shortwave radiative forcing (CRF) is calculated for the surface. CRF is the difference between the net flux when the sky is overcast (index c) and when it is clear (index 0) (Ramanathan et al. 1989, Dong & Mace 2003):

$$\text{CRF} = (E_d^c - E_u^c) - (E_d^0 - E_u^0),\qquad(4)$$

where E_d and E_u are the respective downward and upward fluxes (irradiances/surface density of the flux). The values of CRF are positive for surface warming and negative for surface cooling.

In this paper we analyse the radiative forcing computed for selected spectral channels of the MODIS radiometer. Spectral radiative forcing on 21 June for the spring albedo pattern and for selected MODIS bands are shown in Figure 10a. The daily mean irradiances were computed from values for solar azimuths 0, 90, 180 and 270° on that day and the respective zenith angles. On 21 June, the sun is above the horizon 24 hours in the Hornsund region. The daily mean spectral radiative forcing is expressed as

Figure 10. Relative spectral cloud radiative forcing at the fjord surface on 21 June (a) and at noon on 21 June ($\vartheta = 53°$, $\alpha = 180°$); simulations for $\tau = 12$, cloud base height $h = 1000$ m and spring albedo pattern. Relative radiative forcing is expressed as a fraction of the respective daily mean downward irradiance at the TOA (a) and downward irradiance at the TOA (b). The numbers in the legend are the plot numbers from Figure 4
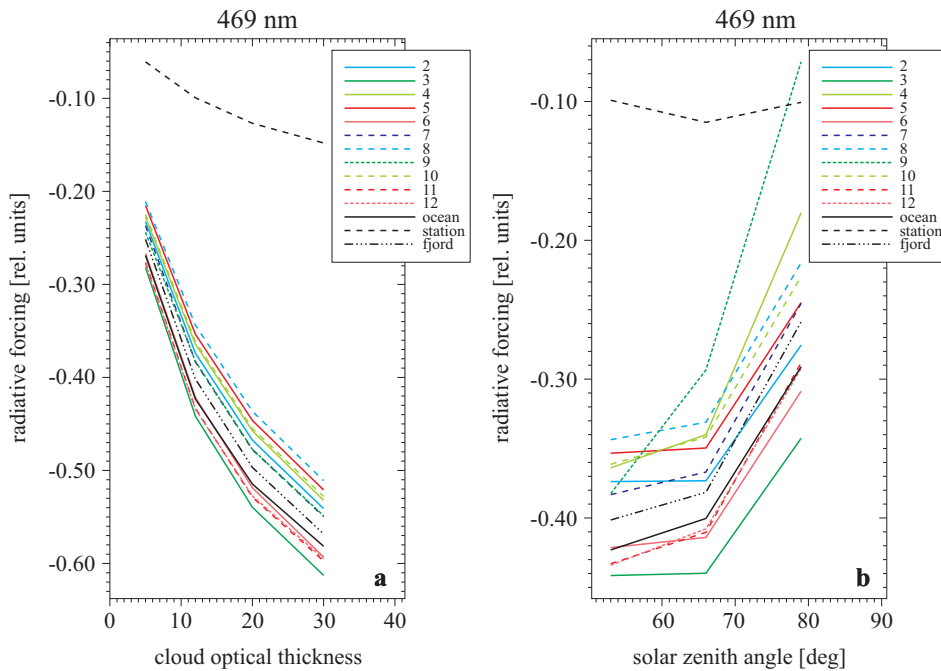
the fraction of the daily mean downward irradiance at the TOA on that day and denoted by $\mathrm{CRF}_{\mathrm{rel}}^{\mathrm{daily}}(\lambda)$.

Radiative forcing $\mathrm{CRF}_{\mathrm{rel}}^{\mathrm{daily}}(\lambda = 469 \text{ nm})$ for a cloud of $\tau = 12$ situated 1 km above the sea surface is -0.396 for the open ocean. For the mouth of the fjord (plot 11) $\mathrm{CRF}_{\mathrm{rel}}^{\mathrm{daily}}(\lambda = 469 \text{ nm})$ is -0.408. $\mathrm{CRF}_{\mathrm{rel}}^{\mathrm{daily}}(\lambda = 469 \text{ nm}) = -0.396$ means that the difference between the amounts of energy absorbed under cloudy and cloudless skies is 0.396 times the daily mean irradiance at TOA. The $\mathrm{CRF}_{\mathrm{rel}}^{\mathrm{daily}}(\lambda = 469 \text{ nm})$ for the whole fjord is -0.370, that is, its magnitude is 0.026 lower than for the open ocean. For other plots (shore adjacent areas) the magnitude of $\mathrm{CRF}_{\mathrm{rel}}^{\mathrm{daily}}(\lambda = 469 \text{ nm})$ is up to 0.1 less than it is for the ocean. This is caused by the much higher downward irradiance E_d under cloudy conditions at the surface of the fjord than at the surface of the open ocean. The greatest differences are found for inner fjords. The magnitude of the daily mean spectral radiative forcing for the station for spring albedo pattern is much lower than for

the fjord, $CRF_{rel}^{daily}(\lambda = 469 \text{ nm}) = -0.09$, because of the highly reflective surface, which reduces the amount of solar energy absorbed by the surface.

The magnitudes of the instantaneous values of spectral radiative forcing $CRF_{rel}(\lambda = 469 \text{ nm})$ computed for the sun's position at noon on 21 June (Figure 10b) ($\tau = 12$, $h = 1$ km, spring albedo pattern, $\vartheta = 53°$, $\alpha = 180°$ and $\lambda = 469$ nm) are higher than the magnitudes of $CRF_{rel}^{daily}(\lambda = 469 \text{ nm})$ for the daily means. $CRF_{rel}(\lambda = 469 \text{ nm})$ is equal to -0.423 for the ocean, -0.401 for the whole fjord, and ranges from -0.34 to -0.37 for the inner fjords (plots 4, 5, and 8). The general pattern, however, is similar except for the plots adjacent to sunlit cliffs. The magnitude of $CRF_{rel}(\lambda = 469 \text{ nm})$ there is higher than it is for the ocean because of the enhanced E_d under a clear sky.
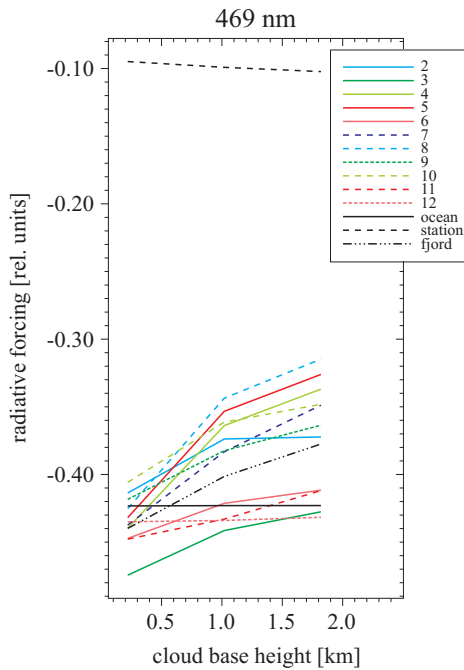
The dependence of $CRF_{rel}(\lambda = 469 \text{ nm})$ on τ is shown in Figure 11a for $\alpha = 180°$, $\vartheta = 53°$ and $h = 1$ km. The magnitude of $CRF_{rel}(\lambda = 469 \text{ nm})$ for the ocean increases from 0.27 for $\tau = 5$ to 0.58 for $\tau = 30$ (note that

Figure 11. Dependence of the relative cloud spectral radiative forcing at the fjord surface on cloud optical thickness (a) and solar zenith angle (b); simulations for $h = 1$ km, spring albedo pattern, $\lambda = 469$ nm (MODIS channel 3), $\alpha = 180°$ and $\vartheta = 53°$ (a) and $\tau = 12$ (b). Relative radiative forcing is expressed as a fraction of the respective downward irradiance at the TOA. The numbers in the legend are the plot numbers from Figure 4

$\mathrm{CRF}_{\mathrm{rel}}(\lambda = 469\ \mathrm{nm}) < 0)$. The magnitude of $\mathrm{CRF}_{\mathrm{rel}}(\lambda = 469\ \mathrm{nm})$ for the whole fjord is lower than that of $\mathrm{CRF}_{\mathrm{rel}}(\lambda = 469\ \mathrm{nm})$ for the ocean by 0.01 to 0.02. The maximum difference, $\Delta\mathrm{CRF}_{\mathrm{rel}}(\lambda = 469\ \mathrm{nm}) = 0.022$, was found for $\tau = 12$. The $\mathrm{CRF}_{\mathrm{rel}}(\lambda = 469\ \mathrm{nm})$ for the whole fjord makes up from 93.5 to 97.7% of the ocean $\mathrm{CRF}_{\mathrm{rel}}(\lambda = 469\ \mathrm{nm})$ value for $\tau = 5$ and 30 respectively. The magnitude of $\mathrm{CRF}_{\mathrm{rel}}(\lambda = 469\ \mathrm{nm})$ decreases with increasing solar zenith angle (Figure 11b), mainly due to the decrease in atmospheric transmittance and for some parts of the fjord (plots 9 and 4) also due to mountain shading. The difference in $\mathrm{CRF}_{\mathrm{rel}}(\lambda = 469\ \mathrm{nm})$ between the whole fjord and the ocean $\Delta\mathrm{CRF}_{\mathrm{rel}}(\lambda = 469\ \mathrm{nm})$ ranges from 0.019 ($\vartheta = 66°$) to 0.032 ($\vartheta = 79°$).

$\mathrm{CRF}_{\mathrm{rel}}(\lambda = 469\ \mathrm{nm})$ and $\Delta\mathrm{CRF}_{\mathrm{rel}}(\lambda = 469\ \mathrm{nm})$ depend strongly on cloud height h in accordance with the dependence of T_E over the fjord on h (Figure 12). For very low clouds ($h = 0.2$) a T_E enhancement over the fjord due to 3D effects is small – smaller than the enhancement for a clear sky. This results in $\Delta\mathrm{CRF}_{\mathrm{rel}}(\lambda = 469\ \mathrm{nm}) = -0.017$. T_E over the fjord for an overcast sky increases with cloud base height but does not depend on h over

Figure 12. Dependence of the relative cloud spectral radiative forcing at the fjord surface on cloud base height; simulations for $\tau = 12$, $\vartheta = 53°$, $\alpha = 180°$, spring albedo pattern and $\lambda = 469$ nm. Relative radiative forcing is expressed as a fraction of the downward irradiance at the TOA. The numbers in the legend are the plot numbers from Figure 4

the open ocean. Therefore the difference in $\mathrm{CRF_{rel}}(\lambda=469\ \mathrm{nm})$ between the fjord and the ocean increases with cloud base height. For $h = 0.5\text{--}0.6$ the $\Delta\mathrm{CRF_{rel}}(\lambda=469\ \mathrm{nm})$ is about 0 and increases up to 0.045 for $h = 1.8$ km.

For the summer albedo pattern the range of spatial variability in $\mathrm{CRF_{rel}}(\lambda=469\ \mathrm{nm})$ is 60% of its value for snow conditions, and cloud radiative forcing for the whole fjord is close to its ocean value (for $\tau = 12$, $\vartheta = 53°$, $\alpha = 180°$, $h = 1$ km and $\lambda = 469$ nm, $\Delta\mathrm{CRF_{rel}}(\lambda=469\ \mathrm{nm}) = -0.004$).

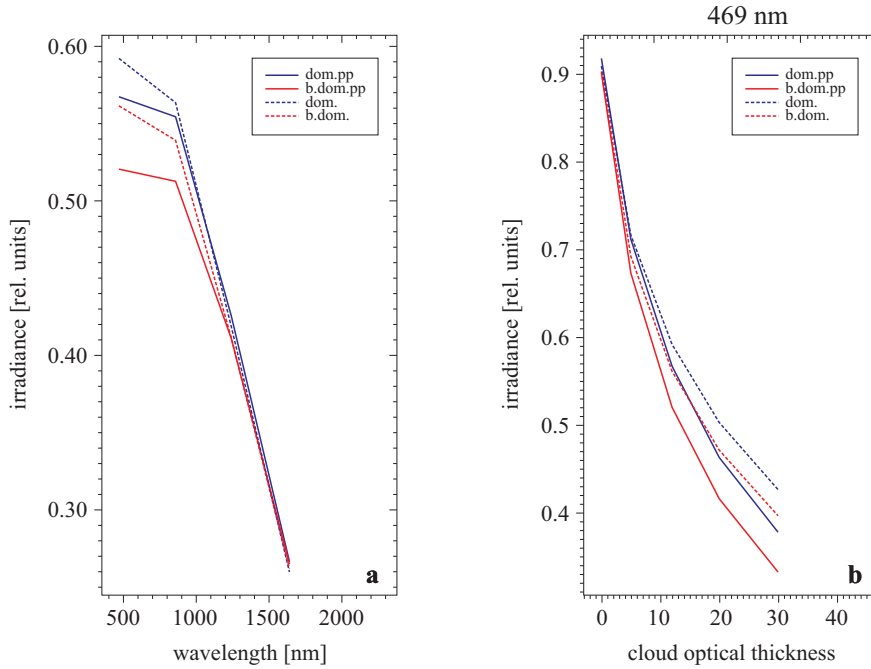Changing g to the ice cloud value ($g = 0.75$) diminishes $\mathrm{CRF_{rel}}(\lambda = 469\ \mathrm{nm})$ (i.e. increases $\mathrm{CRF_{rel}}(\lambda=469\ \mathrm{nm})$ magnitude) but the $\mathrm{CRF_{rel}}(\lambda = 469\ \mathrm{nm})$ span for the plots remains at about 0.1. The difference in $\mathrm{CRF_{rel}}(\lambda=469\ \mathrm{nm})$ for the whole fjord and the ocean decreases slightly to $\Delta\mathrm{CRF_{rel}}(\lambda=469\ \mathrm{nm}) = 0.015$ ($\tau = 12$, $h = 1$ km, spring albedo pattern, $\vartheta = 53°$, $\alpha = 180°$ and $\lambda = 469$ nm).

In general, $\mathrm{CRF_{rel}}(\lambda=469\ \mathrm{nm})$ in the visible and near infrared ($\lambda \leq 1240$ nm) for the fjord is very different from $\mathrm{CRF_{rel}}(\lambda=469\ \mathrm{nm})$ for the ocean under the same conditions. Also, high spatial variability within the fjord is observed. The expected difference between the whole fjord and the ocean is the greatest for clouds of $\tau = 12$ with a high base, a high solar zenith angle and a high land surface albedo (albedo contrast between land and water).

3.3. Anomaly in surface irradiance due to the uniform surface assumption
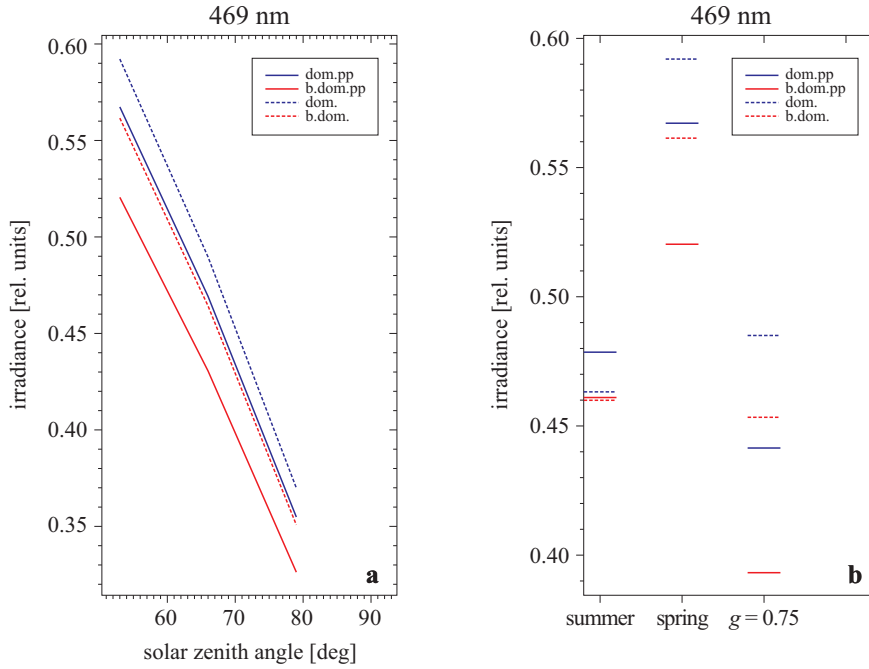
The anomaly in surface irradiance due to the assumption of a uniform surface Δpp_s discussed in this section is the difference between the surface irradiance in the uniform or plane-parallel case, and the slope-parallel irradiance at an actual non-uniform surface with the same mean altitudes of the terrain and the same mean surface albedo, averaged over a given area. The anomaly, expressed as a fraction of the downward irradiance at the TOA, is presented in Figures 13–14 as a function of wavelength (Figure 13a, simulations for $\tau = 12$, $\vartheta = 53°$, $\alpha = 180°$, $h = 1$ km, spring albedo pattern), cloud optical thickness (Figure 13b, simulations for $\vartheta = 53°$, $\alpha = 180°$, $h = 1$ km and $\lambda = 469$, spring albedo pattern), solar zenith angle (Figure 14a, simulations for $\tau = 12$, $\alpha = 180°$, $h = 1$ km and $\lambda = 469$, spring albedo pattern), surface albedo (Figure 14b, simulations for $\tau = 12$, $\vartheta = 53°$, $\alpha = 180°$, $h = 1$ km and $\lambda = 469$) and asymmetry factor of the cloud scattering phase function g (Figure 14b, simulations for $\tau = 12$, $\vartheta = 53°$, $\alpha = 180°$, $h = 1$ km, $\lambda = 469$, spring albedo pattern). The anomaly due to the uniform surface assumption is the equivalent of the surface contribution

Figure 13. Dependence of the anomaly in the relative domain-averaged slope-parallel irradiance due to the uniform surface assumption on solar radiation wavelength (MODIS channels) (a) and cloud optical thickness (b); simulations for $\vartheta = 53°$, $\alpha = 180°$, spring albedo pattern, cloud base height $h = 1000$ m and $\tau = 12$ (a), and $\lambda = 469$ nm (b). The relative surface slope-parallel irradiances are expressed as a fraction of the respective downward irradiance at the TOA. The abbreviation 'dom' stands for the main domain, 'b.dom' for the broad domain and 'pp' for the plane-parallel case

to the plane-parallel bias in cloud transmittance discussed in Rozwadowska & Cahalan (2002). The plane-parallel bias in Rozwadowska & Cahalan (2002) was defined as the difference between the cloud transmittance in the uniform or plane-parallel case and the transmittance under actual non-uniform conditions with the same mean cloud optical thickness and the same mean surface albedo. The anomaly due to the uniform surface assumption reflects errors made in global circulation models, where grid cells are large and averaged conditions for cells are used in the computations. Results are shown for the working domain and 'the broad domain', i.e. the working domain with buffer belts. The respective mean surface elevations for the domain and the broad domain are 173 m and 165 m, the mean spring surface albedos are 0.560 and 0.453 and the mean summer surface albedos are 0.339 and 0.287. The broad domain contains more sea surface than the working domain. Moreover, the vertical borders of the broad domain are cyclic,

Figure 14. Dependence of the anomaly in the relative domain-averaged slope-parallel irradiance due to the uniform surface assumption on solar zenith angle (a) and surface albedo pattern and asymmetry factor g (b); simulations for $\tau = 12$, cloud base height $h = 1000$ m, $\alpha = 180°$ and $\lambda = 469$ and spring albedo pattern (a) and $\vartheta = 53°$ (b). The relative surface slope-parallel irradiances are expressed as a fraction of the respective downward irradiance at the TOA. In (b), (summer) stands for the simulation using the summer albedo pattern, (spring) for the spring albedo pattern and ($g = 0.75$) for the reduced asymmetry factor of the phase function, $g = 0.75$. Simulations for the summer and spring albedo pattern (b) were performed for $g = 0.86$; simulations for $g = 0.75$ (b) were performed for the spring albedo pattern. The abbreviation 'dom' stands for the main domain, 'b.dom' for the broad domain and 'pp' for the plane-parallel case

i.e. a photon leaving the domain through a given wall enters it through the opposite one. Cyclic borders make the simulations representative of a horizontally infinite mosaic of such domains. The borders of the main domain are also transparent to photons but a photon leaving the domain through a given wall does not immediately re-enter it but continues outside the domain. Therefore the results obtained for the main domain are closer to the real situation.

Typically the anomalies Δpp_s in surface irradiance due to the uniform surface assumption are negative except in cases of low surface albedo and very thin clouds or a cloudless sky (Figure 13). A negative anomaly means

that the plane-parallel approximation underestimates the mean irradiance. For clouds with $h = 1$ km, the anomalies of the highest magnitude are found for $\lambda = 469$ nm and $\tau = 30$: $\Delta pp_s = -0.05$ for the domain and $\Delta pp_s = -0.065$ for the broad domain, which is 13 and 19% of the atmospheric transmittance.

The anomaly magnitude decreases with increasing λ (Figure 13a). When $\tau = 12$, the anomalies of the highest magnitude are found for $\lambda = 469$ nm, $\Delta pp_s = -0.04$ for the wide domain and -0.025 for the domain. They become zero or positive for $\lambda > 1240$ nm.

The anomaly magnitudes drop in value with solar angle (Figure 14a) from $\Delta pp_s = -0.025$ for the working domain (for the broad domain $\Delta pp_s = -0.041$) for $\vartheta = 53°$ to $\Delta pp_s = -0.015$ (-0.025) for $\vartheta = 79°$. The relative anomalies (with respect to the mean surface irradiance), however, are almost constant. For the summer albedo pattern (Figure 14b), $\tau = 12$, $h = 1$ km, $\vartheta = 53°$ $\alpha = 180°$, the anomaly becomes 0 (broad domain) or positive (0.15; domain). Changing g to the ice cloud value ($g = 0.75$) does not influence the sign of the anomaly sign but increases its magnitude (Figure 14b).

Simulations show a large increase in the anomaly magnitude for low-base clouds, to $\Delta pp_s = -0.065$ and -0.08 for $\tau = 12$ and $h = 200$ m, for the domain and the broad domain respectively. This is mainly because the cloud base and cloud top are below some mountain peaks, which diminishes the effective cloud optical thickness in the non-uniform case.

The magnitudes of the anomaly in surface irradiance due to the uniform surface assumption are sufficiently high for it to be important for the radiative balance of the area and for estimating cloud radiative forcing. It leads to an underestimation of the surface cloud forcing in the case of plane-parallel approximation.
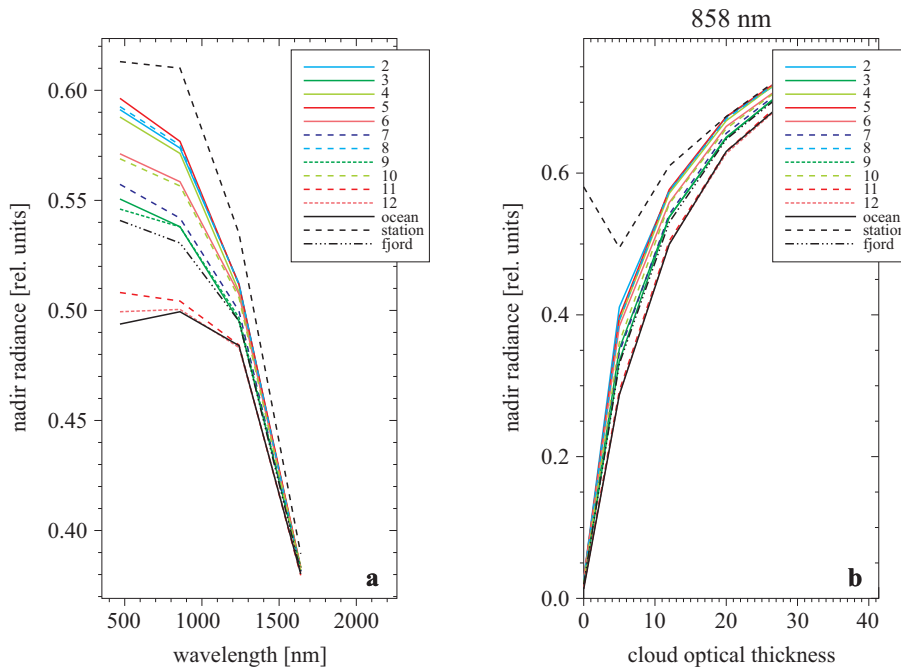
The magnitudes of the anomaly in irradiance at the surface due to the uniform surface assumption Δpp_s found here are higher than the surface contribution to the plane-parallel bias (anomaly) in the atmospheric transmittance (relative downward irradiance) computed by Rozwadowska & Cahalan (2002) for variable Arctic sea ice. The anomaly magnitude for the sea-ice case was < 0.01 for $\tau = 15$, $h = 1.2$ km, $\vartheta = 60°$, $\lambda = 605$ nm and mean surface albedo 0.5. Here, for a mean albedo of ca 0.5, $\tau = 12$, $h = 1$ km, $\vartheta = 53°$ and $\lambda = 469$ nm, the anomaly magnitude is about 0.03. According to studies by Rozwadowska & Cahalan (2002), replacing a uniform cloud layer with thick non-uniform clouds further increases the magnitude of Δpp_s; it may double the anomaly in the case of a mean surface albedo of 0.5. In the case of non-uniform clouds the surface irradiance anomaly (or plane parallel bias) depends on the relative position of thicker parts of the cloud and brighter areas of the surface. When thicker clouds are more likely to

occur over land (for the spring albedo pattern) or glaciers (for the summer albedo pattern), the anomaly (bias) magnitude tends to increase more than it would do so in the opposite situation or in the uncorrelated case.

3.4. Nadir radiance

Channel 2 (858 nm) of the MODIS radiometer combined with channels 7 (2.13 μm) and 20 (3.75 μm) is used for cloud optical thickness and effective particle radius retrieval over the ocean (King et al. 1997). Channel 2 is replaced by channel 1 (0.650 μm) over land and by channel 5 (1.24 μm) over snow and ice surfaces (Platnick et al. 2001, King et al. 2004). The satellite radiance in the visible band depends mainly on cloud optical thickness, whereas the radiance in the absorbing bands for optically thicker clouds is primarily dependent on particle size alone. A combination of visible and near-infrared absorbing bands therefore provides information on both optical thickness and effective radius (King et al. 1997).

A fjord surface without ice is a dark surface, therefore the oceanic algorithm should be used. This section discusses the possible contamination

Figure 15. Dependence of the normalized nadir radiance at the TOA on wavelength (a) and cloud optical thickness (b); simulations for $h = 1$ km, $\vartheta = 53°$, $\alpha = 180°$, spring albedo pattern, and $\tau = 12$ (a) and $\lambda = 858$ nm, MODIS channel 2 (b). The numbers in the legend are the plot numbers from Figure 4

of dark fjord pixels with radiation from the bright land surface surrounding the fjord. Satellite radiances at the TOA for $\lambda = 858$ nm were simulated for various conditions. The TOA radiance shown in this paper is the normalized nadir radiance defined by equation (2). Figure 15b gives the dependence of the nadir radiance on cloud optical thickness for various regions of the Hornsund fjord ($h = 1$ km, $\vartheta = 53°$, $\alpha = 180°$, spring albedo pattern and $\lambda = 858$ nm) and compares it to the open ocean dependence. For the mouth of the fjord and the central part of the fjord the differences between the 'real' nadir radiance and the radiance over the open ocean do not exceed 0.005 for $\tau > 12$ and 0.02 for $\tau = 5$. The radiance enhancement decreases for longer wavelengths. For $\lambda = 1640$ nm it is negligible over the whole fjord (Figure 15a).

If we assume that the cloud microphysics is known (water cloud, droplet effective radius $r_e = 10$ μm) and τ is retrieved solely from channel 858 nm, the error in τ resulting from the application of the oceanic algorithm there is < 1. However, near the shoreline (within 2 km of it), especially over the inner fjords, the differences can exceed 0.12 for $\tau = 5$ and 0.05 for $\tau = 20$ for cloud base height 1 km. These translate to absolute errors in cloud optical thickness retrieval of > 3 for $\tau = 5$ and > 5 for $\tau = 20$.

4. Conclusions

The results of Monte Carlo simulations of the transfer of solar radiation over the Hornsund region showed a considerable impact of the land surrounding the fjord on the solar radiation over the fjord.

The distribution of atmospheric transmittance of downward irradiance on the fjord surface depends on cloud base height, surface albedo and its variability, solar zenith angle, and cloud optical thickness. The greatest absolute differences between atmospheric transmittances on the fjord and on the ocean were found for cloud optical thickness $\tau = 12$, a low solar zenith angle, a high cloud base and the spring albedo pattern. For $\tau = 12$, $\vartheta = 53°$, cloud base height 1.8 km and $\lambda = 469$ nm, the transmittance enhancement is 0.19 for the inner fjords and 0.10 for the whole fjord ($\lambda = 469$ nm). The greatest enhancement relative to the transmittance on the open ocean surface were found for a high cloud optical thickness ($\tau = 30$), a high cloud base and the spring albedo pattern. For $\tau = 30$, $\vartheta = 53°$, cloud base height 1 km and $\lambda = 469$ nm, the relative enhancement is 65% for the inner fjords and 29% for the whole fjord. In summer, especially under clouds with a low base height, the transmittance over the central part of the fjord is close to the oceanic values. Effects of single or multiple reflections between the surface and the clouds are strongly reduced in the infrared. For $\lambda = 1640$ nm, they are negligible. The simulations showed that the

reflection between the Earth's surface and clouds results in considerable spatial variations in atmospheric transmittance (downward irradiance) at the surface in the Hornsund region. Therefore, neither solar radiation measurements performed at the station nor measurements from the open ocean are representative of the fjord.

In this paper we analysed the spectral radiative forcing $\mathrm{CRF}_{\mathrm{rel}}(\lambda)$ computed for selected spectral channels of the MODIS radiometer and expressed as a fraction of the TOA irradiance. Shortwave cloud radiative forcing at the Earth's surface is negative. In general, spectral cloud radiative forcing for the fjord is quite different from CRF for the ocean under the same conditions. Also, a high spatial variability within the fjord is observed. The expected difference between the fjord and the ocean is the greatest for clouds of $\tau = 12$, a high cloud base, spring albedo pattern and a high solar zenith angle. Spectral radiative forcing $\mathrm{CRF}_{\mathrm{rel}}^{\mathrm{daily}}(\lambda = 469 \text{ nm})$ calculated from daily mean irradiances for a cloud of $\tau = 12$ lying 1 km above the sea surface ($\lambda = 469$ nm) is -0.396 for the open ocean and -0.370 for the whole fjord. For other plots (shore adjacent areas) the magnitude of $\mathrm{CRF}_{\mathrm{rel}}^{\mathrm{daily}}(\lambda = 469 \text{ nm})$ is up to 0.1 lower than it is for the ocean. This is caused by the much higher E_d at the fjord under cloudy conditions than E_d for the open ocean. The largest difference was found for the inner fjords. The magnitude of $\mathrm{CRF}_{\mathrm{rel}}(\lambda = 469 \text{ nm})$ for the fjord is the highest for thick clouds with low base. For clouds of low base, $h = 200$ m, and $\tau = 12$ the magnitude of the radiative forcing for the fjord is by 0.017 higher than it is for the ocean ($\lambda = 469$ nm, spring albedo pattern, $\vartheta = 53°$, $\alpha = 180°$). For $h = 0.5$–0.6 the difference is about 0. For the summer albedo pattern, the spatial variability in $\mathrm{CRF}_{\mathrm{rel}}(\lambda = 469 \text{ nm})$ is 60% of its value for spring (snow) conditions and $\mathrm{CRF}_{\mathrm{rel}}(\lambda = 469 \text{ nm})$ for the whole fjord is close to its ocean value (for $\tau = 12$, $\vartheta = 53°$, $\alpha = 180°$, and $h = 1$ km, $\mathrm{CRF}_{\mathrm{rel}}(\lambda = 469 \text{ nm})_{\mathrm{fjord}} - \mathrm{CRF}_{\mathrm{rel}}(\lambda = 469 \text{ nm})_{\mathrm{ocean}} = -0.004$).

The anomaly in the surface irradiance due to the uniform surface assumption Δpp_s is the difference between the surface irradiance for the uniform or plane-parallel case and the slope-parallel irradiance for the actual non-uniform surface with the same mean values of the terrain elevation and the same mean surface albedo, averaged over a given area. In the present paper it is expressed as a fraction of the downward irradiance at the TOA. Typically, the anomaly is negative except for cases of low surface albedo and very thin clouds/a cloudless sky. For clouds with relatively high base (1 km) the anomalies of the highest magnitude are found for $\lambda = 469$, spring albedo pattern, $\vartheta = 53°$ and $\tau = 30$: $\Delta pp_s = -0.05$ for the domain and $\Delta pp_s = -0.065$ for the broad domain, which is 13% and 19% of the atmospheric transmittance of irradiance. The simulations show

a considerable increase in the anomaly magnitude for low-base clouds, to -0.065 (-0.08 for the broad domain) for $\tau = 12$ and $h = 200$ m. This is mainly because the cloud base and cloud top are below some mountain peaks, which diminishes the effective cloud optical thickness in the non-uniform case. The anomaly magnitudes are sufficiently high to be important for the radiative balance of the area and for estimating cloud radiative forcing. In the case of the *pp*-approximation, surface shortwave cloud forcing is typically underestimated.

Channel 2 ($\lambda = 858$ nm) of the MODIS radiometer is used for cloud optical thickness retrievals over the ocean. If we assume that the cloud microphysics is known (water cloud, droplet effective radius $r_e = 10$ μm) and τ is retrieved solely from channel 858 nm, the simulated error resulting from the application of the oceanic algorithm to the cloud optical thickness retrieval is < 1 (low-level clouds, cloud base height 1 km, $\vartheta = 53°$) for the mouth of the fjord and the central part of the fjord. However, near the shoreline (within 2 km of it) and over the inner fjord, the enhancement in the normalized nadir radiance can exceed 0.12 for $\tau = 5$ and 0.05 for $\tau = 20$. This leads to the overestimation of the cloud optical thickness retrieval by > 3 for $\tau = 5$ and by > 5 for $\tau = 20$. The error may be bigger for other than nadir observation angles but such cases were not simulated in this work.

Acknowledgements

References

Arnold N. S., Rees W. G., Hodson A. J., Kohler J., 2006, *Topographic controls on the surface energy balance of a high Arctic glacier*, J. Geophys. Res., 111, F02011, http://dx.doi.org/10.1029/2005JF000426.

Arnold G. T., Tsay S.-C., King M. D., Li J. Y., Soulen P. F., 2002, *Airborne spectral measurements of surface-atmosphere anisotropy for arctic sea ice and tundra*, Int. J. Remote Sens., 23 (18), 3763–3781, http://dx.doi.org/10.1080/01431160110117373.

Baran A. J., Shcherbakov V. N., Baker B. A., Gayet J. F., Lawson R. P., 2005, *On the scattering phase-function of non-symmetric ice-crystals*, Q. J. R. Meteorol. Soc., 131 (611), 2609–2616, http://dx.doi.org/10.1256/qj.04.137.

Benner T. C., Curry J. A., Pinto J. O., 2001, *Radiative transfer in the summertime Arctic*, J. Geophys. Res., 106 (D14), 15173–15183, http://dx.doi.org/10.1029/2000JD900422.

Berk A., Anderson G. P., Acharya P. K., Hoke M. L., Chetwynd J. H., Bernstein L. S., Shettle E. P., Matthew M. W., Alder-Golden S. M., 2003, *MODTRAN4. Version 3. Revision 1. Users manual*, Air Force Res. Lab., Hanscom, AFB, MA., 91 pp.

Błaszczyk M., Jania J., Hagen J. O., 2009, *Tidewater glaciers of Svalbard: recent changes and estimates of calving fluxes*, Pol. Polar Res., 30 (2), 85–142.

Chen Y., Hall A., Liou K. N., 2006, *Application of three-dimensional solar radiative transfer to mountains*, J. Geophys. Res., 111 (D21111), http://dx.doi.org/10.1029/2006JD007163.

D'Almeida G. A., Koepke P., Shettle E. P., 1991, *Atmospheric aerosols. Global climatology and radiative characteristics*, A. DEEPAK Publ., Hampton, 561 pp.

Degünther M., Meerkötter R., 2000, *Influence of inhomogeneous surface albedo on UV irradiance: effect of a stratus cloud*, J. Geophys. Res., 105 (D18), 22755–22761, http://dx.doi.org/10.1029/2000JD900344.

Dong X., Mace G. G., 2003, *Arctic stratus cloud properties and radiative forcing derived from ground-based data collected at Barrow, Alaska*, J. Clim., 16 (3), 445–461, http://dx.doi.org/10.1175/1520-0442(2003)016<0445:ASCPAR>2.0.CO;2.

Dunlap E., De Tracey B. M., Tang C. C. L., 2007, *Short-wave radiation and sea ice in Baffin Bay*, Atmos.-Ocean, 45 (4), 195–210, http://dx.doi.org/10.3137/ao.450402.

Fu Q., 2007, *A new parameterization of an asymmetry factor of cirrus clouds for climate models*, J. Atmos. Sci., 64 (11), 4140–4150, http://dx.doi.org/10.1175/2007JAS2289.1.

Grenfell T. C., Perovich D. K., 1984, *Spectral albedos of sea ice and incident solar irradiance in the southern Beaufort Sea*, J. Geophys. Res., 89 (C3), 3573–3580, http://dx.doi.org/10.1029/JC089iC03p03573.

Grenfell T. C., Warren S. G., Mullen P. C., 1994, *Reflection of solar radiation by the Antarctic snow surface at ultraviolet, visible and near-infrared wavelengths*, J. Geophys. Res., 99 (D9), 18669–18684, http://dx.doi.org/10.1029/94JD01484.

Henyey L. G., Greenstein J. L., 1941, *Diffuse radiation in the galaxy*, Astrophys. J., 93, 70–83, http://dx.doi.org/10.1086/144246.

Hofierka J., 1997, *Direct solar radiation modelling within an open GIS environment*, Proc. JEC-GI'97 conf., Vienna, Austria, IOS Press, Amsterdam, 575–584.

Hu Y. X., Stamnes K., 1993, *An accurate parametrization of the radiative properties of water clouds suitable for use in climate models*, J. Climate, 6 (4), 728–742, http://dx.doi.org/10.1175/1520-0442(1993)006<0728:AAPOTR>2.0.CO;2.

Iwabuchi H., 2006, *Efficient Monte Carlo methods for radiative transfer modeling*, J. Atmos. Sci., 63 (9), 2324–2339, http://dx.doi.org/10.1175/JAS3755.1.

King M. D., Platnick S., Yang P., Arnold G. T., Gray M. A., Riedi J. C., Ackerman S. A., Liou K.-N., 2004, *Remote sensing of liquid water and ice cloud*

optical thickness and effective radius in the Arctic: application of airborne multispectral MAS data, J. Atmos. Ocean. Technol., 21 (6), 857–875, http://dx.doi.org/10.1175/1520-0426(2004)021<0857:RSOLWA>2.0.CO;2.

King M. D., Tsay S.-C., Platnick S. E., Wang M., Liou K.-N., 1997, *Cloud retrieval algorithms for MODIS: optical thickness, effective particle radius, and thermodynamic phase*, MODIS Algorithm Theoretical Basis Document No. ATBD-MOD-05 MOD06 – Cloud product (23 December 1997, version 5), 79 pp.

Kolondra L., 2002, *Problemy fotogrametrycznego pozyskiwania danych w badaniach glacjologicznych (studium metodyczne na przykładzie Spitsbergenu)*, rozprawa doktorska, Biblioteka Wydziału Nauk o Ziemi Uniwersytetu Śląskiego, 166 pp. + 3 mapy.

Kylling A., Dahlback A., Mayer B., 2000, *The effect of clouds and surface albedo on UV irradiances at a high latitude site*, Geophys. Res. Lett., 27 (9), 1411–1414, http://dx.doi.org/10.1029/1999GL011015.

Kylling A., Mayer B., 2001, *Ultraviolet radiation in partly snow covered terrain: observations and three-dimensional simulations*, Geophys. Res. Lett., 28 (19), 3665–3668, http://dx.doi.org/10.1029/2001GL013034.

Liou K. N., Lee W.-L., Hall A., 2007, *Radiative transfer in mountains: application to the Tibetan Plateau*, Geophys. Res. Lett., 34, L23809, http://dx.doi.org/10.1029/2007GL031762.

Lubin D., Ricchiazzi P., Payton A., Gautier C., 2002, *Significance of multidimensional radiative transfer effects measured in surface fluxes at an Antarctic coastline*, J. Geophys. Res., 107 (D19), 4387, http://dx.doi.org/10.1029/2001JD002030.

Marchuk G., Mikhailov G., Nazaraliev M., Darbinjan R., Kargin B., Elepov B., 1980, *The Monte Carlo methods in atmospheric optics*, Springer-Verlag, New York, 208 pp.

Marsaglia G., 1999, *Random numbers for C: The END?*, Message-ID36A5FC62.17C9CC33@stat.fsu.edu in newsgroups sci.math and sci.stat.math, 20 Jan 1999, http://groups.google.com/group/sci.crypt/browse_thread/thread/ca8682a4658a124d/.

Marsaglia G., Zaman A., 1993, *The KISS generator*, Technical report, Florida State Univ., Tallahassee, FL.

Marshak A., Davis A. B. (eds.), 2005, *3D radiative transfer in cloudy atmospheres*, Springer-Verlag, Berlin-Heidelberg–New York, 686 pp., http://dx.doi.org/10.1007/3-540-28519-9.

Marshak A., Davis A., Wiscombe W., Titov G., 1995, *The verisimilitude of the independent pixel approximation used in cloud remote sensing*, Remote Sens. Environ., 52 (1), 71–78, http://dx.doi.org/10.1016/0034-4257(95)00016-T.

Mayer B., Degünther M., 2000, *Comment on 'Measurements of erythemal irradiance near Davis Station, Antarctica: effect of inhomogeneous surface albedo'*, Geophys. Res. Lett., 27 (21), 3489–3490, http://dx.doi.org/10.1029/1999GL011171.

Mayer B., Hoch S. W., Whiteman C. D., 2010, *Validating the MYSTIC three-dimensional radiative transfer model with observations from the complex topography of Arizona's meteor crater*, Atmos. Chem. Phys., 10 (18), 8685–8696, http://dx.doi.org/10.5194/acp-10-8685-2010.

McComiskey A., Ricchiazzi P., Gautier C., Lubin D., 2006, *Assessment of a three dimensional model for atmospheric radiative transfer over heterogeneous land cover*, Geophys. Res. Lett., 33, L10813, http://dx.doi.org/10.1029/2005GL025356.

Ørbæk J. B., Hisdal V., Svaasand L. E., 1999, *Radiation climate variability in Svalbard: surface and satellite observations*, Polar Res., 18 (2), 127–134, http://dx.doi.org/10.1111/j.1751-8369.1999.tb00284.x.

Perovich D. K., Richter-Menge J. A., Jones K. F., Light B., 2008, *Sunlight, water, and ice: extreme Arctic sea ice melt during the summer of 2007*, Geophys. Res. Lett., 35, L11501, http://dx.doi.org/10.1029/2008GL034007.

Pirazzini R., Räisänen P., 2008, *A method to account for surface albedo heterogeneity in single-column radiative transfer calculations under overcast conditions*, J. Geophys. Res., 113, D20108, http://dx.doi.org/10.1029/2008JD009815.

Platnick S., Li J. Y., King M. D., Gerber H., Hobbs P. V., 2001, *A solar reflectance method for retrieving the optical thickness and droplet size of liquid water clouds over snow and ice surfaces*, J. Geophys. Res., 106 (D14), 15185–15199, http://dx.doi.org/10.1029/2000JD900441.

Podgorny I., Lubin D., 1998, *Biologically active insolation over Antarctic waters: effect of a highly reflecting coastline*, J. Geophys. Res., 103 (C2), 2919–2928, http://dx.doi.org/10.1029/97JC02763.

Ramanathan V., Cess R. D., Harrison E. F., Minnis P., Barkstrom B. R., Ahmad E., Hartmann D., 1989, *Cloud-radiative forcing and climate: results from the Earth Radiation Budget Experiment*, Science, 243 (4887), 57–63, http://dx.doi.org/10.1126/science.243.4887.57.

Ricchiazzi P., Gautier C., 1998, *Investigation of the effect of surface heterogeneity and topography on the radiation environment of Palmer Station, Antarctica, with a hybrid 3-D radiative transfer model*, J. Geophys. Res., 103 (D6), 6161–6176, http://dx.doi.org/10.1029/97JD03629.

Ricchiazzi P., Payton A., Gautier C., 2002, *A test of three-dimensional radiative transfer simulation using the radiance signatures and contrasts at a high latitude coastal site*, J. Geophys. Res.-Atmos., 107 (D22), 4650, http://dx.doi.org/10.1029/2001JD001166.

Rozwadowska A., 2008, *Influence of the land topography and cover on the spatial distribution of solar radiation balance components at the land and sea surface in the Hornsund region, Spitsbergen – a pilot model study*, IO PAS internal report, Statutory research task I.1.1, 2008, 23 pp.

Rozwadowska A., Cahalan R., 2002, *Plane-parallel biases computed from inhomogeneous Arctic clouds and sea ice*, J. Geophys. Res., 107 (D19), 4387, http://dx.doi.org/10.1029/2002JD002092.

Shupe M. D., Uttal T., Matrosov S. Y., 2005, *Arctic cloud microphysics retrievals from surface-based remote sensors at SHEBA*, J. Appl. Meteorol., 44 (10), 1544–1562, http://dx.doi.org/10.1175/JAM2297.1.

Shupe M. D., Uttal T., Matrosov S. Y., Frisch A. S., 2001, *Cloud water contents and hydrometeor sizes during the FIRE Arctic Clouds Experiment*, J. Geophys. Res., 106 (D14), 15015–15028, http://dx.doi.org/10.1029/2000JD900476.

Smolskaia I., Nunez M., Michael K., 1999, *Measurements of erythemal irradiance near Davis Station, Antarctica: effect of inhomogeneous surface albedo*, Geophys. Res. Lett., 26 (10), 1381–1384, http://dx.doi.org/10.1029/1999GL900190.

Spada F., Krol M. C., Stammes P., 2006, *McSCIA: application of the Equivalence Theorem in a Monte Carlo radiative transfer model for spherical shell atmospheres*, Atmos. Chem. Phys., 6 (12), 4823–4842, http://dx.doi.org/10.5194/acp-6-4823-2006.

Stamnes K., Tsay S.-C., Laszlo I., 2000, *DISORT, a general-purpose Fortran program for discrete-ordinate method radiative transfer in scattering and emitting layered media: documentation and methodology*, ver. 1.1.

Stamnes K., Tsay S.-C., Wiscombe W., Jayaweera K., 1988, *Numerically stable algorithm for discrete-ordinate-method radiative transfer in multiple scattering and emitting layered media*, Appl. Opt., 27 (12), 2502–2509, http://dx.doi.org/10.1364/AO.27.002502.

Szymanowski M., Kryza M., Migała K., Sobolewski P., Kolondra L., 2008, *Preliminary results of GIS-based solar radiation model for Hornsund area, SW Spitsbergen. The dynamics and mass budget of Arctic glaciers*, Extended abstracts, Workshop and GLACIODYN (IPY) meeting, 29–31 January 2008, Obergurgl (Austria), IASC Working group on Arctic Glaciology, Inst. Marine Atmos. Res., Utrecht Univ., Utrecht, 126–128.

Šúri M., Hofierka J., 2004, *A new GIS-based solar radiation. Model and its application to photovoltaic assessments*, Transactions GIS, 8 (2), 175–190, http://dx.doi.org/10.1111/j.1467-9671.2004.00174.x.

Thomas G., Stamnes K., 2002, *Radiative transfer in the atmosphere and ocean*, Cambridge Univ. Press, Cambridge, 517 pp.

Werenskioldbreen and surrounding areas, Spitsbergen, Svalbard, Norway; orthophotomap 1:25 000, 2002, Uniwersytet Śląski, Wydział Biologii i Nauk o Ziemi, Sosnowiec and Norsk Polarinstitutt, Tromsø, Sosnowiec.

Werner I., Ikävalko J., Schünemann H., 2007, *Sea-ice algae in Arctic pack ice during late winter*, Polar Biol., 30 (11), 1493–1504, http://dx.doi.org/10.1007/s00300-007-0310-2.

Winther J.-G., Gerland S., Ørbæk J. B., Ivanov B., Blanco A., Boike J., 1999, *Spectral reflectance of melting snow in a high Arctic watershed on Svalbard: some implications for optical satellite remote sensing studies*, Hydrol. Process., 13 (12–13), 2033–2049, http://dx.doi.org/10.1002/(SICI)1099-1085(199909)13:12/13<2033::AID-HYP892>3.0.CO;2-M.

Zhang Y., Li Z., Macke A., 2002, *Retrieval of surface solar radiation budget under ice cloud sky: uncertainty analysis and parameterization*, J. Atmos. Sci., 59 (20), 2951–2965, http://dx.doi.org/10.1175/1520-0469(2002)059<2951: ROSSRB>2.0.CO;2.